## PAPER

Check for updates

# Role of ZrO$_2$ in TiO$_2$ composites with rGO as an electron mediator to enhance the photocatalytic activity for the photodegradation of methylene blue†

Lihini Jayasinghe, (ID) Vimukthi Jayaweera, (ID) Nuwan de Silva (ID) * and Azeez M. Mubarak

The development of effective methods to overcome the limitations associated with recombination of photocatalysts used in the treatment of dye effluent are important. In this paper we describe a synthetic pathway to produce reduced graphene oxide (rGO)/TiO$_2$–ZrO$_2$ (GTZ-*X*) composites *via* an *ex situ* solution mixing method without using strong reducing agents. These composites were then compared with rGO/TiO$_2$ (GT) composite, where rGO is used as a suitable support and mediator for the stabilization of semiconductors with a view to overcoming the above limitations. The structural, morphological, optical, and photocatalytic properties of GT/GTZ-*X* were studied using several techniques. X-ray diffraction patterns suggested that a significant amount of GO has been reduced to rGO during the synthesis of composites. The surface analysis data confirms that the pore diameters of the composites are between 3–3.5 nm and can be categorised as mesoporous solids, which positively reflects on their photocatalytic activity. The characterization data confirmed that the metal oxides were successfully incorporated into the rGO sheets while SEM and TEM images display uniformly dispersed spherical morphology of TiO$_2$ and ZrO$_2$ exposing a high number of active sites for enhanced photodegradation. Furthermore, the presence of a Ti–C bond in the deconvoluted C 1s XPS spectrum of the composite confirms bond formation, further supported by Raman and FT-IR spectral data. The photocatalytic performance of the GT/GTZ-*X* composites was evaluated using methylene blue. Compared to the control, the composite with 20 wt% ZrO$_2$ (GTZ-20) showed the highest photocatalytic activity with 95% degradation in 100 minutes with a rate constant of 0.0414 min$^{-1}$, while higher amounts of ZrO$_2$ in composites lowered its photocatalytic activity. Hence, the synthesis of rGO/TiO$_2$–ZrO$_2$ by converting GO to rGO without using strong reducing agents appears to be a promising strategy for preparing mixed metal oxide composite photocatalysts, with enhanced photocatalytic activity.

## Introduction

Many industries such as textile, cosmetic, paper, leather, pharmaceutical, and food generate significant amounts of dye effluents that require an efficient treatment process before being discharged to the environment. Since even trace levels of dyes in treated effluent is undesirable, stringent environmental regulations are in place in many countries to control the discharge of dye waste into the environment. Hence there is an increasing trend globally to develop effective and eco-friendly methods for the removal of dyes from industrial effluents.[1]

*Sri Lanka Institute of Nanotechnology, Nanotechnology and Science Park, Mahenwatte, Pitipana, Homagama, Sri Lanka. E-mail: nuwans@slintec.lk; Fax: +94 11 4741995; Tel: +94 11 4650524*

Conventional wastewater treatment methods include physical, chemical and biological treatments (*e.g.*, coagulation–flocculation and activated carbon adsorption) but these techniques are not effective in removing dyes due to their low molecular weights and high water solubility.[2,3] Biological processes also become inefficient when industrial effluents contain toxic and/or non-biodegradable organic substances.[4] In recent years, Advanced Oxidation Processes (AOPs) have been developed to remove the contaminants from effluents.[5] This process is based on the generation of very reactive species such as hydroxyl radicals ($^{\bullet}$OH) that can oxidize a broad range of organic pollutants quickly and non-selectively.[6]

Among the existing processes, semiconductor material mediated photocatalysis is considered to be highly promising and efficient due to its low cost and higher efficiency toward eliminating both organic and inorganic pollutants.[7–10]

Semiconductor particles with an appropriate band gap are the most efficient for photocatalysis due to their filled valence bands and empty conduction bands.[11] Titanium dioxide (TiO$_2$), the most effective semiconductor photocatalyst for the photodegradation of organic pollutants in water, has shown promising applications in wastewater purification owing to its nontoxic, chemically inert, photostable characteristics, and low production cost.[12–14] However, TiO$_2$ has a low photocatalytic efficiency due to the rapid recombination of photogenerated electron–hole pairs caused by its large band gap energy (3.2 eV for anatase and 3.0 eV for rutile) that cannot absorb visible light.[7] Therefore, researchers are currently focused on developing effective methods to overcome the issues associated with recombination of electron–hole pairs especially without the use of strong reducing agents.[15] One such pathway is the synthesis of new semiconductor hetero-structure systems that have different properties, promoting charge separation, suppressing charge recombination and broadening the spectral range of light absorption, compared to the individual components.[16,17]

In addition to TiO$_2$, another n-type semiconductor material zirconium dioxide (ZrO$_2$) has also attracted attention due to its biological and chemical ineffectiveness, non-toxicity, and safety.[18] ZrO$_2$ ($\sim 5.0$ eV), when coupled with TiO$_2$, exhibits enhanced photo-degradation properties.[19–21] It has been reported that the addition of small amounts of ZrO$_2$ into TiO$_2$ can decrease the crystallite size of TiO$_2$ due to the dissimilar nuclei and coordination geometry and these mixed oxides have been extensively used as catalysts for a wide variety of reactions.[22] TiO$_2$–ZrO$_2$ mixed oxide composites are used as photocatalysts due to a reduced bandgap in comparison to their individual components.[23–27] They are known to exhibit a high surface acidity due to an imbalance of charges resulting from the formation of the Ti–O–Zr bridges.[27] The main advantage of the addition of ZrO$_2$ to TiO$_2$ is that it increases the mobility of electrons and stabilizes the phase transformation of anatase into rutile, thus increasing the material's thermal stability. Moreover, the interaction between these two components leads to the creation of new active catalytic sites, which is important in the photocatalytic approach.[24,28–31]

However, low adsorption and surface area are the two most important limitations of photocatalytic efficiency, therefore efforts have been made to stabilize the semiconductors on suitable supports to overcome these limitations. It was envisaged that these nanoscale systems will increase separation of charges, lifespan of the charge carriers, charge surface transfer to adsorbent substrates and also reduce costs.[32]

To overcome such complications, graphene has emerged as a promising matrix material to be used as a substrate of a high specific surface area in TiO$_2$/ZrO$_2$-based composites. Graphene, a 2-D nanomaterial with a sp$^2$ carbon network, is a zero-band gap semiconductor that has an extremely high conductivity (5000 W m$^{-1}$ k$^{-1}$) and theoretical surface area (2630 m$^2$ g$^{-1}$) and can provide very high mobility to photogenerated electrons and reduce e$^-$/h$^+$ recombination.[33] Graphene oxide (GO) by having plenty of chemical functionalization on its surface and edges acts as an excellent supporting material for metal oxides. The addition of graphene has also been shown to cause a red-shift in the absorption spectrum leading to activation of photocatalysts under visible-light irradiation.[34]

Among examples of semiconductor oxides and other materials examined with TiO$_2$/ZrO$_2$ and rGO, g-C$_3$N$_4$,[35,36] WO$_3$,[37] ZnO,[38] ZnV$_2$O$_4$,[39] MXenes,[40] SnO$_2$,[41] and Nb$_2$O[42] have displayed significant potential. Each one of the materials forming such composites display a different chemical interaction with the contaminant to decompose. Composite materials synthesised to overcome common limitations such as low surface area and fast recombination rate may show improved photocatalytic activity but it is of great importance to innovate cost effective and environment friendly methods of synthesis that do not compromise their photocatalytic performance. Therefore, this study aims to provide novel insight and an important step forward to enhance efficiency with an economic and environmentally sustainable photocatalytic system for dye degradation. We report a novel *ex situ* synthesis of ZrO$_2$-based reduced graphene oxide (rGO)/TiO$_2$ composites by a solution mixing method combined with a weak reducing agent for the GO–rGO conversion. These nanoscale systems effectively decrease the band gap of TiO$_2$ and ZrO$_2$ and simultaneously restrict the e$^-$/h$^+$ pair recombination through increasing the e$^-$ conductivity of the system. The synthesized materials were then used as active photocatalysts in heterogeneous photo degradation and their photocatalytic dye degradation efficiency in the presence of UV light is assessed using the cationic industrial dye Methylene Blue (MB) used in textiles and ink manufacturing. There has been many literature reports studying the influence of varying percentage content of rGO and TiO$_2$ in mixed metal oxide composites but for the first time to the best of our knowledge we report the influence of different loading of ZrO$_2$ in rGO/TiO$_2$ composites on the degradation of MB and the efficiency and degradation rate of these photocatalysts compared with a composite consisting of only rGO/TiO$_2$.

# Experimental section

## Materials

All chemical reagents were procured from commercial sources and used without further purification. Titanium dioxide (anatase, 99.8% trace metals basis), ZrO$_2$ (99% trace metals basis), ethanol (reagent grade, 99.8%), and potassium permanganate (KMnO$_4$) (ACS reagent, $\geq$99.0%) from Sigma Aldrich. Sodium hydroxide pellets (extra pure AR, 98%), sulfuric acid (H$_2$SO$_4$) (extrapure AR, 98%), hydrogen peroxide (H$_2$O$_2$) (extrapure AR, 99.5%), hydrochloric acid (HCl) (extrapure AR, 98%), diethyl ether (extrapure AR, 99.5%), and methylene blue (MB) from Sisco Research Laboratories. Natural vein graphite ($>$99%) was supplied by Kahatagaha Graphite Lanka Limited (KGLL).

## Preparation of GT/GTZ-*X* composites

GO was synthesized following our own patented methodology; a modified chemical oxidation method that converts graphite

to GO using $H_2SO_4$ and $KMnO_4$, and then quenching the reaction mixture with $H_2O_2$ and ice.[43]

1.5 g of natural vein graphite was weighed in a vessel and 100 mL $H_2SO_4$ was added while maintaining the temperature at 0 °C. 5.4 g of $KMnO_4$ was then added to the mixture at a rate of 2 g min$^{-1}$, while stirring. The stirring continued for 12 h while maintaining the temperature of the mixture between 0–10 °C. Once the colour turned to dark brown, the reaction mixture was quenched with 200 g of ice, and then 1.5 mL of $H_2O_2$. The mixture was allowed to settle and the supernatant was discarded leaving a GO slurry, which was washed several times starting with deionized water followed by a 1 : 2 water : HCl mixture to remove $Mn^{2+}$ ions and other impurities. Final washing was carried out with ethanol:diethyl ether (1 : 1) mixture to obtain brown GO powder, which was then dried at room temperature under vacuum for 3 h.

The synthesis of all composites was then carried out by varying the content of $ZrO_2$ (5 wt%, 10 wt%, 20 wt%, 30 wt%, and 40 wt%) while maintaining the GO : $TiO_2$ ratio at 10 wt% to obtain composites with different rGO-Ti-to-Zr ratios. An *ex situ* solution mixing method, a method generally adopted for the synthesis of rGO/metal oxide photocatalysts, was used to make the composites.[44]

The synthesis of the composites was performed in two steps. First, an appropriate amount of GO was dispersed in 200 mL of distilled water and sonicated for 30 min. Separately, appropriate quantities of $TiO_2$ and $ZrO_2$ were dispersed in distilled water and sonicated for a period of 20 min. This mixture was then added into the GO solution, magnetically stirred at 300 rpm and sonicated for 30 min. 20 mL of 1 M NaOH solution was then added drop-wise into the sonicated mixture and the resultant mixture was stirred for 2 h at 100 °C, during which time the colour of the mixture changed to black qualitatively indicating the successful reduction of GO to rGO. The synthesized rGO/$TiO_2$–$ZrO_2$ composites were harvested by centrifuging at 3000 rpm for 10 min and the residue was washed first with 60% ethanol and then distilled water three to four times. The washed product was finally calcined at 250 °C for 6 h and dried under vacuum. The composites were stored in amber colour vials at room temperature under dry and dark conditions until used. A composite consisting of only rGO and $TiO_2$ were synthesized similarly and used as the control in this study.

The samples were denoted as GT (rGO/$TiO_2$ control) and GTZ-$X$; where $X$ is the wt% of $ZrO_2$ present in the composite. For example, the sample with 40 wt% of $ZrO_2$ was denoted as GTZ-40.

### Characterizations

The X-ray diffraction (XRD) patterns of GO, $TiO_2$, $ZrO_2$, GT and GTZ-$X$ composites were acquired using a Bruker, Focus D8 X-ray diffractometer equipped with a Cu-K$\alpha$ source (40 kV, 40 mA, $\lambda = 3$). The diffracted beam intensities were recorded from 5° to 90° at a scan speed of 10.0 degrees minute$^{-1}$ at $2\theta$ angles. The morphology of GT and GTZ-$X$ composites was studied using a transmission electron microscope (TEM, JEOL JEM-2100; 200 kV accelerating voltage) and scanning electron microscope

(SEM). SEM analysis was performed on GT and GTZ-$X$ powders on a carbon tape in a scanning electron microscope (SEM) (Hitachi SU6600) at an accelerating voltage of 10 kV. The elemental analysis was carried out using the SEM equipped with an Oxford Instruments INCA $x$-sight energy dispersive X-ray detector (EDAX).

Fourier transform infrared (FTIR) spectra of the composites were obtained in the 600 cm$^{-1}$ to 4000 cm$^{-1}$ wave number range using Bruker, Vertex 80 in Attenuated total reflectance (ATR) mode. A Bruker Senterra Raman Microscope with an argon ion laser at 532 nm wavelength with 50× lens for excitation was used to record the Raman spectra.

The surface areas of the samples were determined from nitrogen adsorption–desorption isotherms at liquid nitrogen temperature using a surface area analyser (Quantachrome autosorb iQ with ASiAwin software) and the pore size distribution (pore diameter and volume) was determined by the Barrett–Joyner–Halenda (BJH) method.[45] Samples for BET analysis were dried in a drying oven at 80 °C overnight and then degassed at 300 °C for 360 min prior to the analysis. HPLC monitoring was carried out using a Shimadzu LC-20AP preparative HPLC system. X-ray photoelectron spectroscopic (XPS) analysis was carried out using a Thermo Scientific TM ESCALAB Xi+ equipped with a monochromated Al K$\alpha$ X-ray source and a resistive anode detector.

Band gap energies of GT and GTZ-$X$ composites were determined using solid phase diffuse reflectance UV spectra (Shimadzu UV-3600) with Kubelka-Munk transformations.

### Photocatalytic measurements

The photocatalytic activities of different composites were estimated by monitoring the degradation of MB in a home-made apparatus under UV light (254 nm). Aqueous solution was maintained at 25 °C throughout the experiment and the time dependent adsorption–desorption of the photocatalysts was evaluated in darkness for 100 min before irradiation.

25 mg of photocatalyst was added to 50 mL MB solution (60 µg mL$^{-1}$) in a reactor and the suspension was magnetically stirred for 0.5 h to reach the adsorption/desorption equilibration without UV or visible-light exposure. After irradiation, 4 mL aliquots were withdrawn at fixed time intervals (0, 5, 10, 10, 20, 30, 35, 40, 50, 60, 70, 80, 90, 100 min), filtered through a membrane filter (pore size 0.45 mm) and the absorbance was recorded over the 200–800 nm wavelength range. As a control, the experiment was repeated with rGO/$TiO_2$ (GT) as the photocatalyst. The photocatalytic decolourization of MB was expressed as a function of relative concentration of MB solution ($C/C_0$) computed at $\lambda_{max}$ of MB – 664 nm with reaction time; where $C_0$ is the initial concentration of MB and $C$ is the concentration of MB at time – $t$. Since $\ln C_0/C = kt$, the linear relationship between the logarithm of the relative concentration of MB ($\ln C_0/C$) with the irradiation time was used to estimate the decolourization rate constant ($k$) of the photocatalyst used in the photocatalytic reaction.[46–49]

The reusability of the photocatalyst GTZ-20 was carried out by performing photocatalytic experiments consecutively for

three runs. Each run was exposed to irradiation for 100 min and the photocatalyst was recovered and reused with fresh MB solution. The photocatalytic efficiencies ($D$) were calculated from the equation as shown below and the results are presented in Table 2.

$$\left(\frac{C_0 - C}{C_0}\right) \times 100\% \qquad (1)$$

where, $C_0$ is the initial concentration before photodegradation and $C$ is the concentration after irradiating for 100 min.

The rate constants of the degradation process and the half-life of MB were calculated according to the Langmuir–Hinshelwood equation[42] as shown:[48,49]

$$r = \frac{dC}{dt} = k\left(\frac{KC}{1 + KC}\right) \qquad (2)$$

Considering that the elimination of MB is a pseudo-first-order reaction,[48–50] the reaction rate constant can be determined as the slope of the linear regression:

$$-\ln\frac{C_t}{C_0} = kt \qquad (3)$$

where $k$ is the rate of degradation of MB (min$^{-1}$), $K$ is the equilibrium constant of the adsorption of dye on the surface of the catalyst, and $C_0$ and $C_t$ are the concentrations of MB in aqueous solution before ($t = 0$) and after irradiation for $t$ min. Knowledge of the reaction rate constant, $k$, makes it possible to determine the half-life of the dye ($t_{1/2}$) using eqn (4):

$$t_{\frac{1}{2}} = \frac{\ln 2}{k} \qquad (4)$$

## Results and discussion

### Structure and morphology of GT/GTZ-X composites

The XRD patterns of GO, GT, GTZ-20, TiO$_2$ and ZrO$_2$ shown in Fig. 1, revealing that the addition of GO has no change in the diffraction pattern of TiO$_2$. The significant peaks for anatase TiO$_2$ can be observed at $2\theta$ values of 25.01, 37.82, 48.22, 53.83, 55.43, 62.63, 69.03, 70.64 and 75.44 corresponding to (101), (112), (200), (105), (211), (204), (116), (220), and (215) of the anatase phase crystal planes.[51–53] The absence of a strong (002) peak at $2\theta = 10.5°$ for GO in GT and a weak peak in GTZ-20, suggests that a significant amount of GO has been reduced to rGO during the synthesis of the composites.

In the XRD pattern of GTZ-20, those signifying the formation of tetragonal ZrO$_2$ crystals are observed at $\sim 24°$, 28°, 31°, 34°, 49°, 60° and 66° and those signifying the formation of anatase TiO$_2$ are observed at $\sim 25°$, 48°, 75°, and 83°. Peaks at 54°, 55° and 62° in the GTZ-20 XRD pattern are common to both TiO$_2$ and ZrO$_2$. After the synthesis of the GTZ-20 composite, the distinct peak in GO shows a reduced intensity and becomes broader due to the partial breakdown of the long-range order of the GO.[54] The disappearance of the diffraction peak of rGO may be due to rGO being covered with Zr doped TiO$_2$ to a
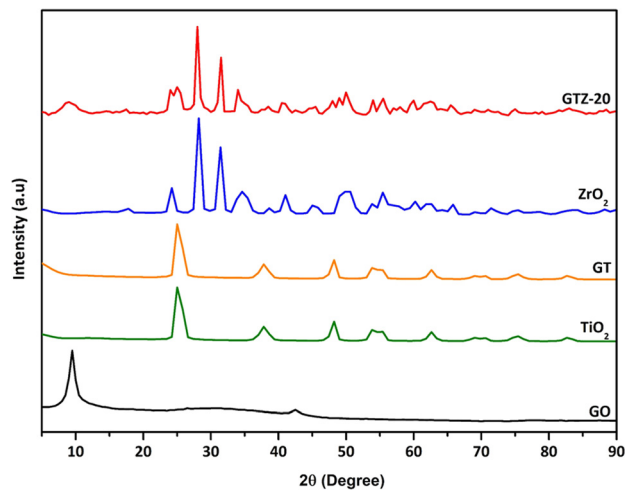


**Fig. 1** XRD patterns of GO, TiO$_2$, ZrO$_2$, GT and GTZ-20.

considerable extent during the synthesis. These results also suggest partial reduction of GO to rGO.

The average crystallite sizes of GT and GTZ-20 composites were calculated using Scherer's equation based on the full width at half maximum (FWHM) of the anatase TiO$_2$ (101) peak.[55]

$$D_{hkl} = \frac{K\lambda}{\beta \cos\theta} \qquad (5)$$

Here, $D_{hkl}$ is the crystallite size, $K$ is a numerical factor frequently referred to as the crystallite-shape factor, $\lambda$ is the wavelength of X-ray radiation, $\beta$ is the full width at half-maximum, and $\theta$ is the diffraction angle.

The crystallite size of pure TiO$_2$, GT and GTZ-20 was $\sim 9.88$, and 8.43 and 4.86 nm respectively as shown in Table 1. This means that as hypothesized the composite formation has decreased the crystallite size of TiO$_2$ in the order TiO$_2$ > GT > GTZ-20 due to dissimilar nuclei and coordination geometry.[56]

Specific surface area, pore radius and pore volume of TiO$_2$, GT and GTZ-20 calculated by the multipoint Brunauer-Emmett-Teller (BET) method are also listed in Table 1. The adsorption/desorption isotherms along with the Barrett–Joyner–Halenda (BJH) pore-size distribution plot are shown in Fig. S2 (ESI†). According to the BET results, TiO$_2$ has a BET specific surface area of 123 m$^2$ g$^{-1}$ with a pore volume of 0.441 cm$^3$ g$^{-1}$. It was also noted that incorporation of metal oxide(s) into the composites has a significant reduction in both specific surface areas and pore volumes (GT-109 m$^2$ g$^{-1}$ and 0.352 cm$^3$ g$^{-1}$;

**Table 1** Surface analysis data from BET analysis and values calculated using Scherer's equation

| Name | Crystallite size (nm) | Pore radius (Å) | Pore volume (cm$^3$ g$^{-1}$) | BET surface area (m$^2$ g$^{-1}$) |
|---|---|---|---|---|
| TiO$_2$ | 9.88 | 61.3 | 0.441 | 123 |
| GT | 8.43 | 15.3 | 0.352 | 109 |
| GTZ-20 | 4.86 | 17.1 | 0.170 | 98 |

GTZ-20-98 $m^2$ $g^{-1}$ and 0.170 $cm^3$ $g^{-1}$ respectively). The presence of agglomerates and decrease in crystallite size in the composite samples (GT and GTZ-20) is consistent with the trend that a small pore volume and surface area is often associated with agglomeration.[57] According to IUPAC classification, microporous and macroporous materials have pore diameters smaller than 2 nm and greater than 50 nm respectively, while the pore diameters of the mesoporous category lie in the middle.[58] Since the pore diameters of both GT and GTZ-20 fall in the range of 3–3.5 nm they can be categorised as mesoporous solids, which positively reflects their photocatalytic activity.

In order to evaluate the effect of the different conditions employed in the synthetic process, the morphology of the samples was further studied by SEM and TEM. Fig. 2(g and h) shows SEM images depicting the influence of $ZrO_2$ incorporated into the GTZ-20 composite. For comparison purposes, SEM images of $ZrO_2$ and $TiO_2$ are also presented in Fig. 2(a–d). The SEM image of GT (Fig. 2(e and f)) revealed that the $TiO_2$ particles adhered on the surface of rGO sheets, and they also seem to be fairly agglomerated. When $ZrO_2$ was incorporated into the composite during the formation of the GTZ-20, these particles too appear to be adhered onto the rGO sheets.
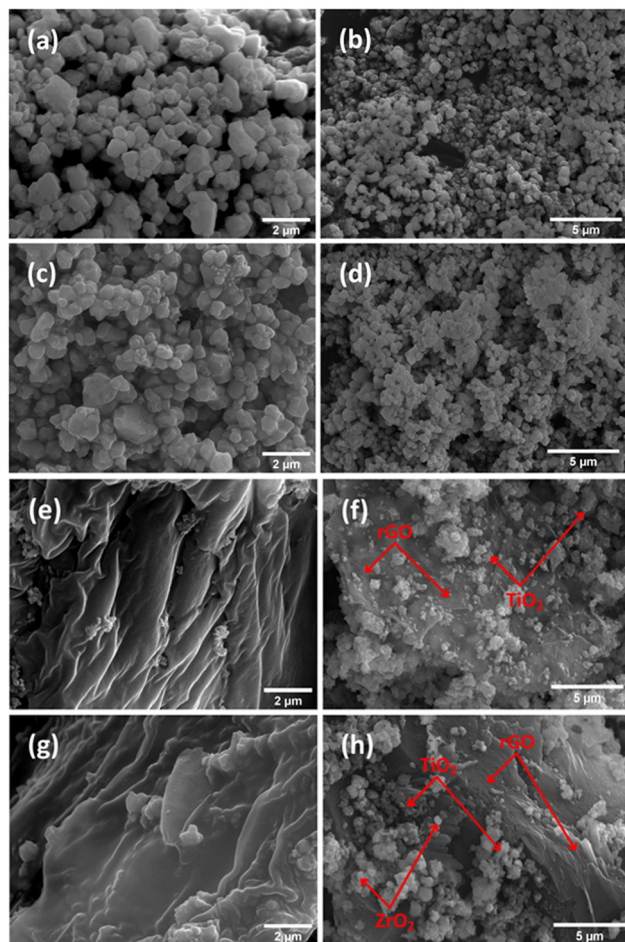
Images show that the as-prepared sample consisted of minor agglomerates of almost spherical crystalline particles. Agglomeration is a common phenomenon observed in $ZrO_2$-$TiO_2$ based composites prepared by an impregnation method.[56] The TEM images of GT (Fig. 3(a and b)) and GTZ-20 (Fig. 3(c and d)) display uniformly dispersed spherical morphology of $TiO_2$ nanoparticles on rGO sheets. The images of GTZ-20 also clearly indicate that the metal oxides are homogeneously dispersed on the surface of individual rGO sheets with little agglomeration. Although some slight aggregation was observed on the graphene sheets after the synthesis process, the overall morphology mostly showed a distributed and uniform state. The deposition of particles on rGO in the composite has little effect on the morphology of rGO, which retained its sheet-like structure. The materials presented sheet-like structures that exposed a high number of active sites for enhanced photo degradation. Selected area electron diffraction (SAED) was performed on the GTZ-20 composite and the corresponding SAED image is shown in Fig. 3e. The EDAX data revealed the presence of O (49.5%), C (14.8%) and Ti (35.7%) in GT composite (Fig. 4a) confirming that the composite did not contain any other component other than C, O, and Ti. Similarly, the EDAX data of GTZ-20 (Fig. 4b) indicated the presence of O (62.2%), Ti (19.6%), C (12.3%) and Zr (5.9%), thus supporting the formation of GTZ composites.

XPS analysis was carried out on GT and GTZ-20 composites (Fig. S1, ESI†) to assess the surface composition, GO to rGO reduction efficiency, oxidation states and interaction between $TiO_2$, $ZrO_2$ and rGO. The survey spectrum and narrow scans of GTZ-20 are shown in Fig. 5. A decrease in C 1s and O 1s peaks corresponding to the oxygenated species with a simultaneous increase in the C–C peak intensity confirms the reduction of GO
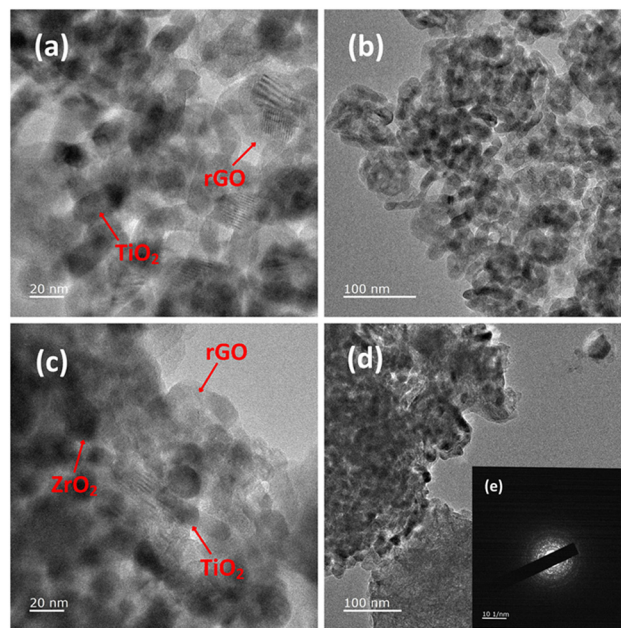


Fig. 2 SEM images of $TiO_2$ nanoparticles (a and b), $ZrO_2$ (c and d), GT (e and f) and GTZ-20 (g and h).



Fig. 3 TEM images of GT (a and b), and GTZ-20 (c and d) under different magnifications and SAED pattern of GTZ-20 (e).
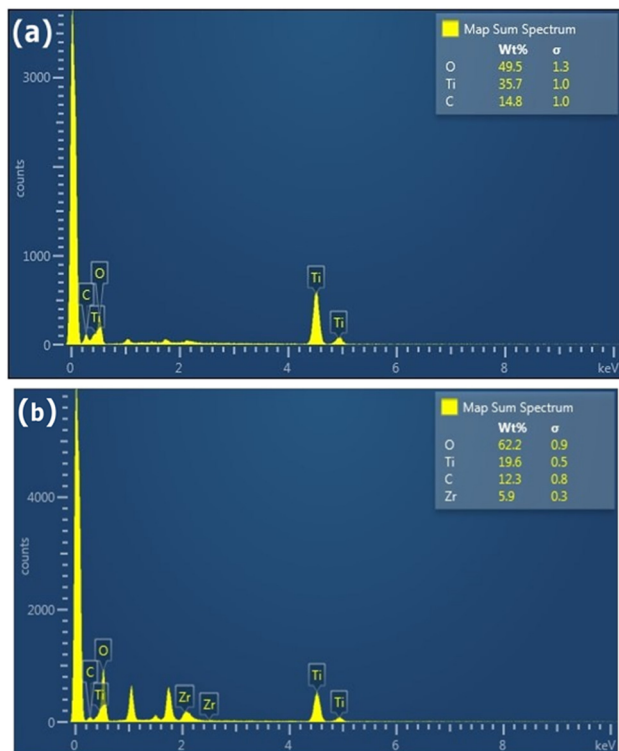
**Fig. 4** EDX analysis of GT (a) and GTZ-20 (b).

to rGO (Fig. 5d).[59] FT-IR analysis of the composites also support the reduction of GO to rGO in the composite.

The survey spectra (Fig. 5a) clearly indicates the presence of, O 1s, Ti 2p, Zr 3d, and C 1s species on the surface of the composite, confirming the successful formation of GTZ-20. The rGO-TiO$_2$ interactions in the composite were also investigated using XPS. The deconvoluted C 1s XPS spectrum (Fig. 5b) shows two types of carbon bonds; C–C at 284.4 eV and Ti–C at 283.8 eV.[60–62] The presence of a Ti–C bond in the composite confirms bond formation in GTZ-20, which was further supported by the Raman and FT-IR spectral data.

As shown in Fig. 5c, the peak at 529.8 eV indicates the existence of the Ti–O–Ti bonds in GTZ-20.[63,64] The weak O 1s peak at 531.5 eV related to Ti–O–C[21,65] may be due to the high proportion of TiO$_2$ when compared to GO in the composite. The two strong characteristic peaks at 458.6 eV and 464.0 eV of Ti 2p (Fig. 5d) are attributed to Ti 2p$_{3/2}$ and Ti 2p$_{1/2}$,[63,66] respectively, which support the binding energies of Ti$^{4+}$ in the TiO$_2$ lattice. Zirconium 3d spectra (Fig. 5e) clearly shows the most prominent peak at 181.8 eV corresponding to Zr 3d$_{5/2}$ and low intense peak at 184.2 eV corresponding to the Zr 3d$_{3/2}$ peak, which suggest that zirconia is in the Zr$^{4+}$ oxidation state. The XPS results suggest that the TiO$_2$ and ZrO$_2$ are chemically bonded with the rGO matrix and not physically adsorbed.

Raman spectroscopy was carried out to obtain more information on the sample structure, composition effects and the features of phase transition of the synthesized composites. Both GT and GTZ-20 samples showed a similar pattern characteristic to the TiO$_2$ anatase phase peaks; the structure of the semiconductor anatase phase has six Raman active modes $(A_{1g} + 2B_{1g} + 3E_g)$[67,68] and five of these modes have been
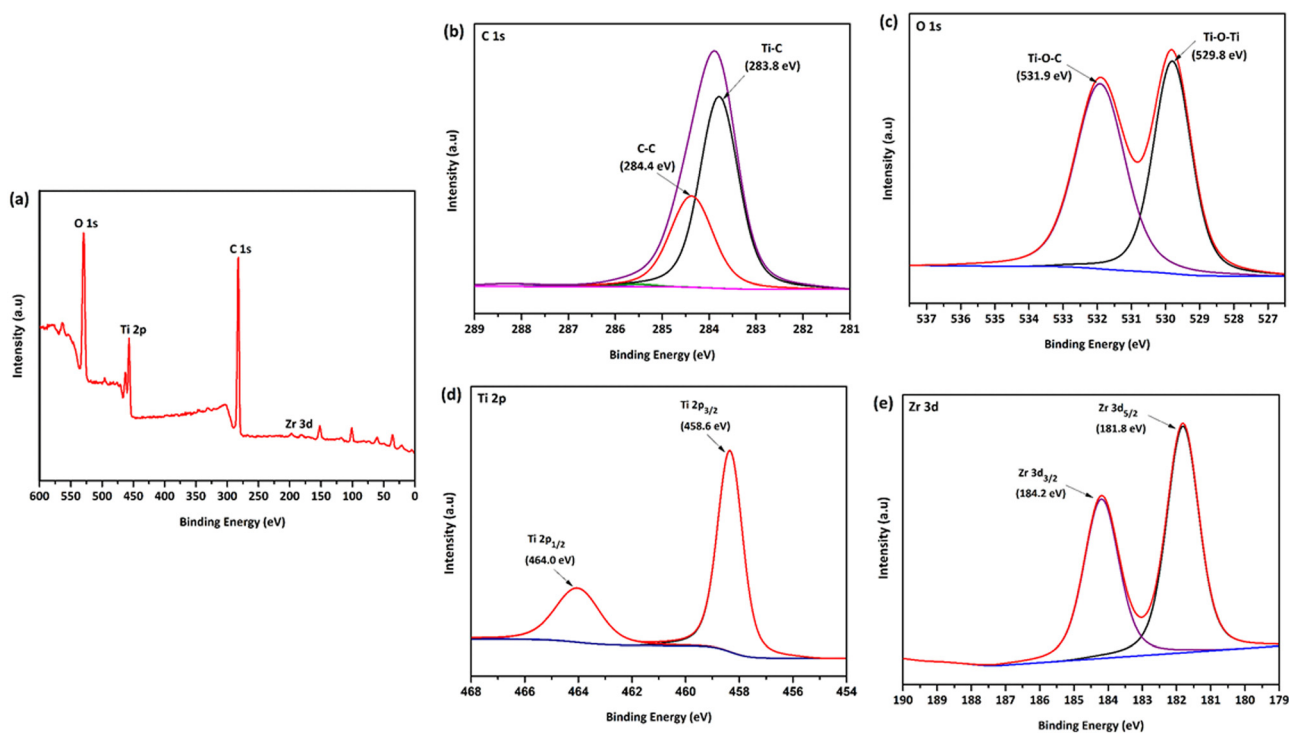


**Fig. 5** XPS survey spectrum (a) of the GTZ-20 composite and its corresponding high-resolution XPS spectra of C 1s (b), O 1s (c), Ti 2p (d) and Zr 3d (e).

detected in the Raman spectra of the GT composite. The Raman spectra of both samples show a strong signal localized at 147 cm$^{-1}$, which is caused by the external vibration of the TiO$_2$ anatase structure. The specific vibration modes are located at 147 cm$^{-1}$ (E$_g$), 393 cm$^{-1}$ (B$_{1g}$), 511 cm$^{-1}$ (A$_{1g}$ + B$_{1g}$) and 632 cm$^{-1}$ (E$_g$) indicating the presence of the anatase phase in all of these samples. The signal localized at 510 cm$^{-1}$ is a double-signal corresponding to modes A$_g$ and B$_{1g}$. Finally, none of the Raman bands corresponding to the TiO$_2$ rutile phase were detected in the spectra. When 20 wt% ZrO$_2$ is incorporated into the composite, titania and zirconia peaks seem to have overlapped, which indicates the successful incorporation of the mixed oxides onto the graphene surface. It is known that zirconia exists as three polymorphs: monoclinic (m-ZrO$_2$), tetragonal (t-ZrO$_2$), and cubic (c-ZrO$_2$). However, no Raman bands at 224, 292, 324, 407, 456 and 636 cm$^{-1}$ due to tetragonal ZrO$_2$ or at 183, 301, 335,381, 476, 536, 559, 613 and 636 cm$^{-1}$ due to monoclinic ZrO$_2$ were observed.[69]

The G peak at ~1580 cm$^{-1}$ and D peak at ~1330 cm$^{-1}$ in both spectra are characteristic of partially reduced GO. The $I_D/I_G$ ratio of GT (1.10) and GTZ-20 (1.00) indicates the transition from sp$^2$ to sp$^3$ due to the presence of more defects of graphene present in both composites.

Fig. 6b shows FT-IR spectra of both GT and GTZ-20 composites. Due to the extensive oxidation of GO, it has a strong and broad O–H stretching vibration band at 3410 cm$^{-1}$, carboxyl C═O stretching band at 1721 cm$^{-1}$, O–H deformation vibration band at 1404 cm$^{-1}$ and C–O stretching vibration at 1087 cm$^{-1}$.[70-73] As expected, these characteristic bands of GO are relatively weaker in the FTIR spectra of GT and GTZ-20 confirming the reduction of GO to rGO during the composite synthesis.

The peaks found at 1603 and 1640 cm$^{-1}$ are resonance peaks that can be assigned to the stretching and bending vibration of OH groups of water molecules adsorbed on titanium dioxide or zirconium dioxide (Ti–OH or Zr–OH) and the peak at ~1382 cm$^{-1}$ arises from the C–OH group.[74] These surface oxygen containing functional groups causes the possibility of covalent linkage of TiO$_2$ and ZrO$_2$ on the GO surface.

GT shows a broad peak at 593 cm$^{-1}$ attributed to the vibration of Ti–O–Ti bonds in TiO$_2$.[75-77] Broad bands or peaks below 1000 cm$^{-1}$ in composites generally indicate a combination of Ti–O–Ti and Ti–O–C vibrations due to the chemical interaction of TiO$_2$ with rGO.[78] The presence of Ti–O–C bonds indicates that GO, with residual carboxyl groups, strongly interacts with the surface hydroxyl groups of TiO$_2$ nanoparticles and forms chemical bonds in the composites during composite formation.

In the FT-IR spectra of GTZ-20 (Fig. 6b), different absorption peaks appeared in the range 1000–500 cm$^{-1}$ due to metallic connections M–O–M, O–M–O or M–OH (M = Zr, Ti). It has also been reported that the bands that appeared in the spectra (400–1200 cm$^{-1}$) characterized the metallic connection M–O–M, O–M–O or M–OH (where in this case M = Zr or Ti).[79] The strong absorption band at 594 cm$^{-1}$ can be assigned to the vibrations of the Zr–O or Ti–O functional groups, but separate elucidation of bands related to Zr–O–Ti, Zr–O–Zr or Ti–O–Ti is not possible for mixed compositions. Finally these results suggest that the existence of interfacial contact between ZrO$_2$, TiO$_2$ and rGO can lengthen the lifetime of photo-generated electron–hole pairs and thereby enhance the photocatalytic activities of GT and GTZ-20 composites.

The interaction of Ti and Zr in the composites was examined by the UV-visible diffusive reflectance spectrometry (UV-vis DRS). The reflectance spectra were transformed to Kubelka–Munk coordinates (KM, α) and then the Tauc plot was constructed (eqn (1)) to estimate the band gaps of the samples.[55,80] According to Fig. 7a, all samples showed an absorption below 450 nm. Addition of ZrO$_2$ to rGO/TiO$_2$ showed stronger absorption intensities for GTZ-30, GTZ-20 and GTZ-10 composites and the enhanced visible light absorption continued even in the 380–700 nm range for both GTZ-20 and GTZ-10 composites.
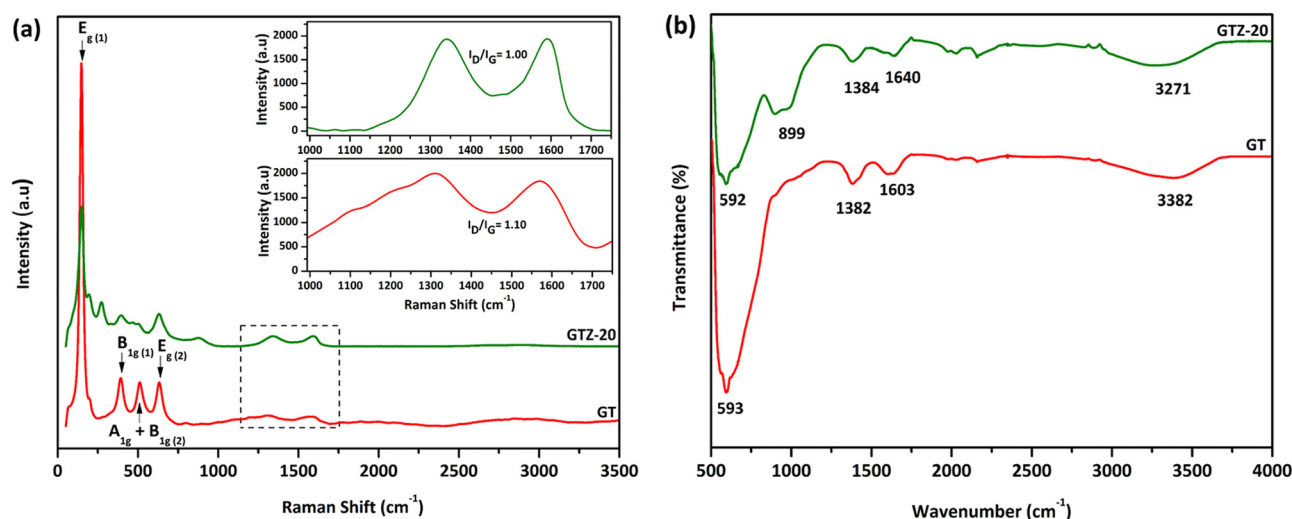


Fig. 6 Raman spectroscopy of GT and GTZ-20. The inset shows D and G bands of GT and GTZ-20 (a); FT-IR spectroscopy of GT and GTZ-20 (b).
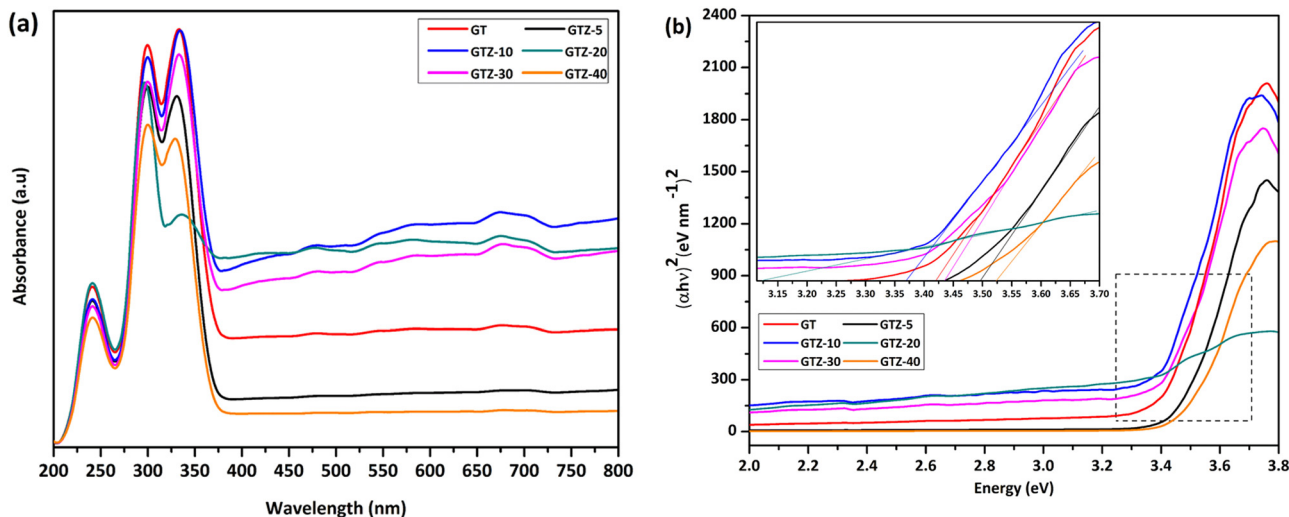
Fig. 7 Solid state UV-vis spectra of GT and GTZ-X composites (a), and band gap estimation using a Tauc plot (b).

Hence incorporation of 10 and 20 wt% $ZrO_2$ to GT has resulted in photocatalytic activity in visible light due to the reduction in band gaps, as observed for other carbonaceous materials combined with metal oxides such as $TiO_2$.[81–83] On the other hand GTZ-40, GTZ-30 and GTZ-5 responded only to ultraviolet (UV) light, which is in agreement with its wide band gap as summarized in Table 3 (3.52 eV, 3.50 eV and 3.44 eV respectively).

The extension of the absorption range of GTZ-X composites upon the addition of $ZrO_2$ above 5 wt% and below 40 wt% suggests a band gap narrowing, which could be caused by the existence of Ti–O–C and Zr–O–C bonding between $TiO_2$, $ZrO_2$ and some specific sites of GO.[84,85] These bonding interactions can accelerate the photoinduced charge transfer from the metal oxides to rGO, which leads to enhancement in the photocatalytic activity of the catalyst. The existence of M–O–Z (M:Ti or Zr) bonding can be further explained by the FT-IR and XPS data (Fig. 6b and 5). The electronic structure of the GT/GTZ-X composites are characterized by energy band gap structure ($E_g$), which is essentially the energy gap between the valence band ($E_v$) and the conduction band ($E_c$). We have calculated the $E_g$ of GT/GTZ-X composites from the absorbance data as shown in Fig. 7(a and b).[86,87] The $E_g$ of the composites were determined by employing the Tauc relationship as given below:

$$(\alpha h\nu)^n = A(h\nu - E_g) \tag{6}$$

where, $\alpha$ is the absorption coefficient (2.303 A $t^{-1}$), $A$ is the absorbance and $t$ is the thickness of the cuvette, $h$ is Planck's constant, $\nu$ is the photon frequency, $E_g$ is the electronic band gap, and $n$ has values of $\frac{1}{2}$ and 2, for direct and indirect transition respectively. From $(\alpha h\nu)^2$ versus $h\nu$ curves, the band gap was evaluated by stretching the linear region of the plot on $h\nu$-axis and finding the intercept. This investigation for $n = 2$, suggested that the transitions were indirect transitions. An extrapolation of the linear region of a plot of $(\alpha h\nu)^2$ on the $Y$-axis versus photon energy ($h\nu$) on the $X$-axis gives the value of

the $E_g$ as shown in Fig. 7b. From these $(\alpha h\nu)^2$ versus $h\nu$ plots, direct optical band gap values of these films are found at 3.42, 3.45, 3.36, 3.12, 3.44 and 3.52 eV for GT, GTZ-5, GTZ-10, GTZ-20, GTZ-30 and GTZ-40 respectively.

A noticeable reduction in the band gaps was observed in GTZ-20 and GTZ-10. The band gap of GT (3.42 eV) decreased when Zr doping was above 5 wt% and below 30 wt% due to the introduction of defects in rGO/$TiO_2$ with the inclusion of Zr. As shown in Fig. S3 (ESI†), the band gap value decreased in the composites even with respect to the band gap of their individual metal oxides, $TiO_2$ (3.53 eV) and $ZrO_2$ (4.40 eV). The decrement, as theorised, can occur with higher Zr-doping due to the creation of localized levels near the conduction band providing a large number of electrons to reach the conduction band,[88] improvement in the crystallinity of the composite structure and defects produced by $Zr^{4+}$ in the $TiO_2$ lattice or enhancement in crystal domains.[89,90] Oxygen functionalization has also been identified to tune the bandgap of graphene.[91] So, in the presence of some oxygen containing functional groups such as (-OH) and (-COOH) in graphene oxide, some unpaired π-electrons bonded with the free electrons on the surface of $TiO_2$ forming a Ti–O–C structure as observed in the acquired characterization information, which shifted up the valence band edge thus reducing the band gap. In addition, we can suppose that the formed Ti–O–Ti bond can also participate in the reduction of the band gap of $TiO_2$. In recent years, the imminent energy crisis and growing pollution concerns, increased the interest in the utilization of renewable energy sources, such as solar. However, most photocatalysts can be activated only by ultraviolet light energy. Ideal materials for photocatalysis should possess features such as high photocatalytic performance toward the near UV and visible region for efficient solar energy utilization.[92] The band gap of the composites indicate the lowering of the band gaps of the composites to as low as 3.12 eV thus expanding the light-harvesting region of the synthesized composites such as

GTZ-20 from UV to visible. Placement of a large percentage of Zr beyond 20% into the TiO$_2$ lattice shifted the conduction band upwards, which increased the optical band gap. A defect band may have been created by oxygen vacancies induced by Zr doping that overlaps with the conduction band of TiO$_2$. This enhancement of the band gap was governed by the Burstein-Moss effect.[93] An increased concentration of charge carriers due to the high percentage of Zr blocks the lowest conduction band state and then electron transitions took place to higher energy states.

The deviation from linearity in the low energy region (Fig. 7b) was initially investigated by Urbach and is frequently identified as the ''Urbach Tail'' and the associated energy as Urbach energy. The lowering of band gap in the composites is due to the presence of localized defect states in the band gap of the respective metal oxides.[94,95]

In an ideal material with absolutely no Urbach tail, the value of $(\alpha h\nu)^2$ would be zero up to the optical gap but this is not the case in real materials where there is always a certain amount of sub-gap absorption. In many amorphous and semi-crystalline materials, it is hypothesized that the exponential dependence of the energy arises from random fluctuations of the internal field, which involve structural disorder and electronic transitions between localized states.[96] The Urbach energy ($E_u$) specifies the width of the localized states in the band gap and it is considered as a parameter containing the effects of all possible defects and depends on the degree of structural disorders.[97,98] Urbach energies of the composites were calculated by the following equation:

$$\alpha h\nu = \beta \exp\left(\frac{h\nu}{E_u}\right) \tag{7}$$

where $\alpha$ is the absorption coefficient, $\beta$ is a constant called the band tailing parameter, $E$ is the photon energy and $E_u$ is the Urbach energy. For the calculation of Urbach energy, $\ln\alpha$ is plotted against $E$. The reciprocal of the slope of linear portion, below optical band gap, gives the value of $E_u$. Since the absorption coefficient $\alpha$ is proportional to absorbance $A$, we can plot $\ln\alpha$ *vs.* photon energy, $E$.[99]

According to the results obtained (Fig. 8), the Urbach energies of the composites are 0.13, 0.29, 0.20, 1.06, 0.29 and 0.13 eV for GTZ-10, GTZ-20, GTZ-30 and GTZ-40 respectively. It is observed that the values of EU increased from 0.13 (Control, GT) following the incorporation of ZrO$_2$ into the composites. The behaviour of $E_U$ in our study shows a certain inverse relationship to the band gap—composites with lower band gaps have higher $E_u$, for example the lowest band gap (3.12 eV) of GTZ-20 also reports the highest Urbach energy which further confirms the enhanced photocatalytic efficiency due to the disorder and defects that have introduced localized states at or near the conduction band level.

High photocatalytic activities of graphene-based metal oxides and mixed metal oxides have been reported previously.[23,44,100–102] In this study, we have assessed the photocatalytic activity of GT/GTZ-*X* photocatalysts to demonstrate their efficacy (Fig. 9).
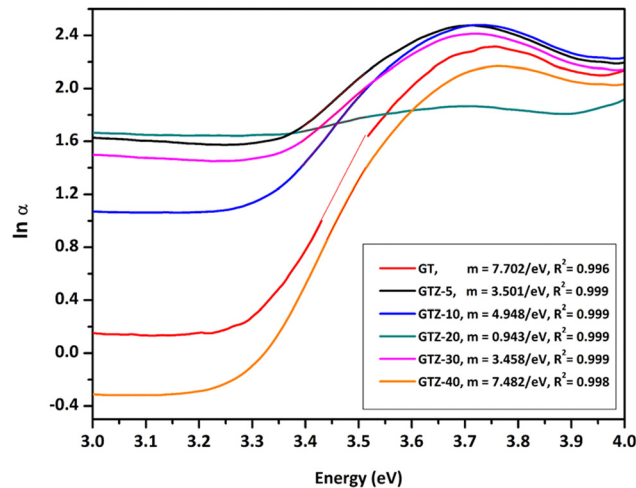


**Fig. 8** Urbach energy plot; plot of (ln α) as a function of photon energy (*E* = *hv*).
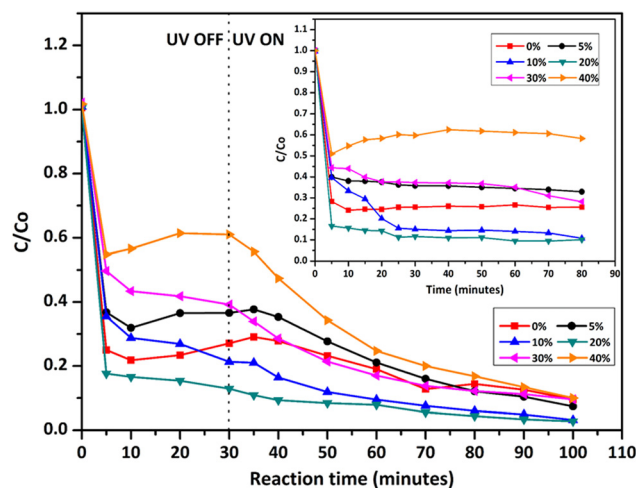


**Fig. 9** Photodegradation of methylene blue under UV irradiation, comparing the performance of GT/GTZ-*X* composites. The inset shows the adsorption tests of GT/GTZ-*X* composites under dark conditions.

Before the photocatalytic tests, the adsorption properties of the synthesized catalysts were evaluated by measuring the absorbance of MB in the presence of catalysts, in the dark, at different time intervals (Fig. 9 – inset). The photodecolourization of MB solution in the presence of the photocatalysts under UV light is shown in Fig. 9. For comparison purposes GT was chosen as the reference photocatalyst. The absorbance of MB depends on the adsorption–desorption equilibrium of MB molecules between the aqueous medium and the catalyst surface. It can be seen that GTZ adsorbed a higher amount of MB than GT, with GTZ-10 and GTZ-20 exhibiting the highest adsorption capacity. Absorbance vs time graphs suggest that, in the dark, the adsorption–desorption equilibrium is reached after 30 min. The equilibrium time was further confirmed by analysing the first derivative of the photocatalytic data (Fig. S5, ESI†). Once the photocatalyst was exposed to UV light after 30 min, there can be seen a gradual decrease in the concentration of MB with time (Fig. 9).

A three step mechanism has been proposed for the degradation of pollutants during photocatalysis – adsorption of the pollutant, absorption of light by the photocatalyst, and charge transfer reactions to create radical species to decompose the pollutants.[100] These three steps can be clearly identified in Fig. 9. GTZ-20 and GTZ-10 showed the best performance with respect to degradation, approximately 95% and 89% of MB was degraded respectively within 100 min while the control GT had a degradation efficiency of only 56.3% (Table 3). Out of all composites GTZ-40 showed the poorest degradation. Fig. 10 clearly shows the decrease in intensity of $\lambda_{max}$-664 nm, the characteristic absorbance band of MB, due to photodecomposition over the GTZ-20 composite when exposed to UV-light.

The photocatalytic degradation can be described with the Langmuir–Hinshelwood equation.[103] Determination of degradation rate constant could be used to quantify the photocatalytic activities of the composites prepared in the present study.[21] The degradation rate constants ($k$) of MB (Fig. 11) were calculated as 0.0414 min$^{-1}$ and 0.0263 min$^{-1}$ for GTZ-20 and GT respectively (Table 3). These results indicate that $k_{GTZ-20}$ and $k_{GTZ-10}$ are much higher than that of all other composites, and $k_{GTZ-20}$ is almost double the value of the control GT. Hence it appears that within a certain % range, the presence of $ZrO_2$ in rGO/TiO$_2$ increases the photocatalytic performance of the composite significantly. A possible explanation being the incorporation of $ZrO_2$ between 10–20 wt% has enabled the formation of more active sites for the adsorption of reactant molecules resulting in the improved photocatalytic degradation performance of GTZ-10 and GTZ-20. The degradation performance of the composites is consistent with the degradation trend of MB. The $t_{1/2}$ (min) of MB with GT-10 and GTZ-20 are 18.84 and 16.73 respectively, which is almost twice as fast as that of the control GT (26.36). Hence GTZ-X composites (GTZ-10 and GTZ-20) synthesized by the method outlined here can be used for the photo-degradation of MB dyes and likely for other organic pollutants as well.
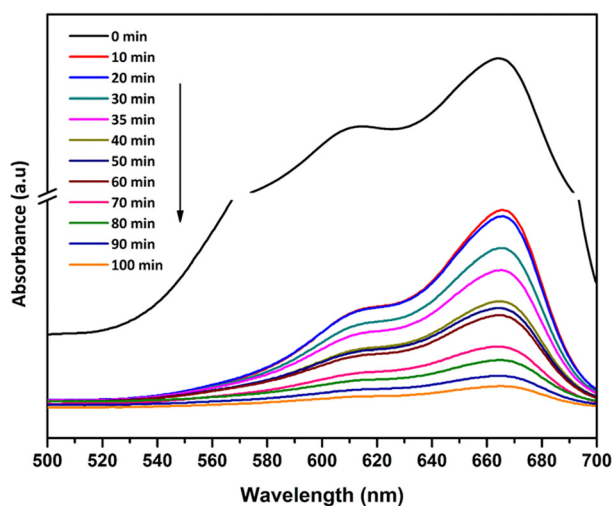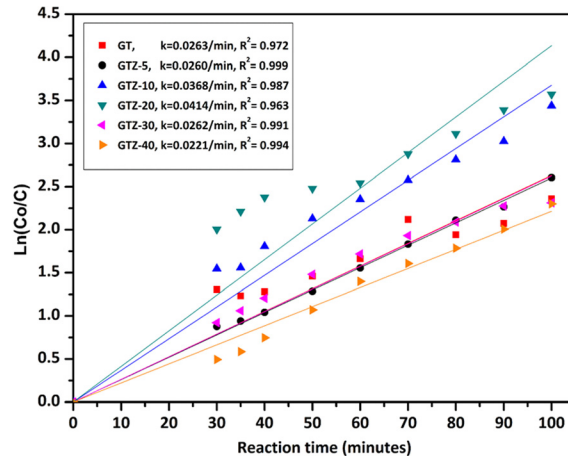


Fig. 11 Linear relationship between the logarithms of the relative concentration of MB solution.

In order to evaluate the reusability of the photocatalysts, a simple experiment was performed utilising the GTZ-20 composite and the results are displayed in Table 2. The initial efficiency ($\geq$96%) of the photocatalyst remained the same during the second run while there was only a slight reduction in efficiency during the third run. By the fifth run, the efficiency had only dropped to 91.6%. Hence the said zirconia-based composites have good potential as photocatalysts for various applications.

The decolourization of dyes is not an indication that the dyes have been completely oxidized into the final products such as $CO_2$ and $H_2O$. Since the oxidation of dyes can lead to the generation of colourless by-products, LC-MS analysis was carried out on the MB solution taken out from the reaction mixture at 0, 30 and 100 min, which was subjected to photodegradation in the presence of GT and GTZ-X composites as described earlier, to identify the by-products formed during degradation and the LC-MS chromatograms are shown in Fig. S4 (ESI†). The chemical structures assigned to the peaks observed in the MS chromatograms are given in Fig. 12. LC-MS results indicate that, prior to UV light exposure, only MB was present in the aqueous solution and no other N-demethylation products. Furthermore, the reaction solution with the GT composite had MB as the dominant component at 30 minutes (no UV) while at 100 minutes it had only N-demethylation product, thionin (Fig. 12b), suggesting that GT has been successful in breaking down the dye photocatalytically.

Although GTZ-20 also showed a similar degradation pathway at 30 minutes (no UV), at 100 minutes it showed, instead of the



Fig. 10 Absorption spectra of Methylene blue in the presence of GTZ-20 with time.

Table 2 Reusability of GTZ-20 in the photodecolourization of the MB solution after 100 min in the presence of UV light

| Run # | D% |
|---|---|
| 1 | 96.6 |
| 2 | 96.5 |
| 3 | 94.5 |
| 4 | 92.6 |
| 5 | 91.6 |

a) Methylene Blue (m/e=284)

b) Thionin (m/e=228)

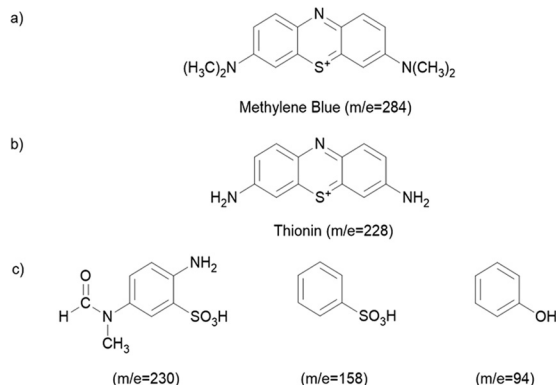c) (m/e=230)    (m/e=158)    (m/e=94)

**Fig. 12** Chemical structures of the degraded products according to the LC-MS chromatograms. Products found in the solution containing GT with time (a and b), and GTZ-20 (c).

*N*-demethylation product (only a small peak of thionin), several other degradation products with *m/z* values of 230, 158, and 94[104,105] (Fig. S4, ESI†) suggesting that GTZ-20 has a stronger photodegradation power than GT with and without UV-light irradiation.

It is observed that GTZ-20 displays strong photodegradation activity due to a decrease in electron–hole recombination and efficiently photodegraded surface adsorbed molecules into smaller fragments.

A possible mechanism for the photocatalytic degradation of MB on GT/GTZ-20 composites under UV-light is shown schematically in Fig. 13. Photocatalysis is based on the activation of a semiconductor (SC) by the sun or artificial light. When an SC material is irradiated with photons whose energy is higher or equal to its band gap energy, an electron jumps from the valence band (VB) to the conduction band (CB) with the concomitant generation of a hole in the VB.[104] The increased photodegradation of MB by GTZ-20 and GTZ-10 can be explained by the presence of an optimum amount of $ZrO_2$ that is required to enable the creation of new phases dispersed in $TiO_2$ for the trapping of the photogenerated ($e^-/h^+$) pairs,
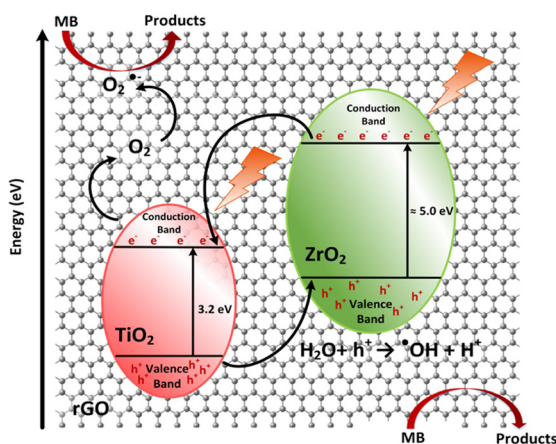
thereby avoiding the recombination of $e^-/h^+$ pairs. As reported, the separation of an electron and hole may take place between $ZrO_2$ and $TiO_2$ in the binary oxide since the energy level of $TiO_2$ both for the VB and CB correspond well within the band gap of $ZrO_2$.[105] Therefore, when irradiated by a photon that is energetically superior to the band gap energy of semiconductors, excited electrons of $ZrO_2$ and $TiO_2$ migrate from their respective VB to CB, generating $e^-/h$ pairs. The created energy levels act as electron capture centres, helping in the separation of the photogenerated ($e^-/h^+$) pairs. However, an excess of defects favours the recombination process, decreasing the photoactivity, which may be the case for GTZ-5, GTZ-30 and GTZ-40 composites. As shown in Fig. 13, when the electrons are excited from both catalysts, most of the electrons from the CB of $ZrO_2$ can easily transfer to the CB of $TiO_2$ and, thereby, the electron–hole recombination may be prevented in $ZrO_2$ (10–20 wt%) loaded to $TiO_2$.

After that, some of the photogenerated electrons ($e^-$) of $ZrO_2$ are captured by the CB of Ti $O_2$, whereas holes ($h^+$) from $TiO_2$ are trapped by the VB of $ZrO_2$, helping to decrease the recombination process by improving the charge separation. Moreover, interfacial carrier separations take place with the help of rGO. Owing to the high conductivity of rGO it is able to act as a sink to trap electrons as a result of the difference in work function of both materials.[106,107] rGO behaves as a solid electron mediator, trapping and transporting electrons in the composite so it was observed that the increase in efficiency depends on the efficient electron transfer and not on the surface area of the BET,[108] as rGO creates a conductive layer of efficient channels at the interface between the $ZrO_2$ and $TiO_2$ to promote electron transport preventing the recombination of photogenerated electron–hole pairs ($e^-/h^+$), which leads to improved photocatalytic activity (Table 3).[109,110]

Since the CB work function of $TiO_2$ matches with the CB work function of graphene, as reported elsewhere,[100] electrons can be easily transfer from CB of $TiO_2$ to rGO. It is known that the chemical reduction of GO only partially restores the $sp^2$ hybridized network and hence the remaining oxygen sites are still able to accept electrons and undergo reduction. As a result, the oxygen sites can readily accept the electrons and undergo a reduction reaction to generate more $O_2^{\bullet-}$ radicals.[111,112] Thus, the presence of rGO in the photocatalyst can produce an excess amount of reactive $O_2^{\bullet-}$ radicals due to the good electron acceptor and transporter behaviours of rGO. Therefore, the ultrafast transportation of photogenerated electrons over the



**Fig. 13** Proposed diagram of the photocatalytic mechanism for rGO/TiO$_2$ based ZrO$_2$ composites.

**Table 3** Catalytic degradation with band gap energies of the composites

| Photocatalyst | Band gap (eV) | Urbach energy, $E_u$ (eV) | $k$ (min$^{-1}$) | $R^2$ | $t_{1/2}$ (min) | % Degradation |
|---|---|---|---|---|---|---|
| GT | 3.42 | 0.13 | 0.0263 | 0.972 | 26.36 | 56.3 |
| GTZ-5 | 3.45 | 0.29 | 0.0260 | 0.999 | 26.66 | 64.1 |
| GTZ-10 | 3.36 | 0.20 | 0.0368 | 0.987 | 18.84 | 89.2 |
| GTZ-20 | 3.12 | 1.06 | 0.0414 | 0.963 | 16.73 | 94.7 |
| GTZ-30 | 3.44 | 0.29 | 0.0262 | 0.991 | 26.46 | 64.4 |
| GTZ-40 | 3.52 | 0.13 | 0.0221 | 0.994 | 31.36 | 43.7 |

rGO sheet can directly reduce $O_2$ to produce $O_2^{\bullet-}$ radicals which leads to enhanced MB degradation.

On the other hand, the $h^+$ from $TiO_2$ captured by the VB of $ZrO_2$ is now totally available to carry out the oxidation reaction of $H_2O$ to produce hydroxyl radicals ($^{\bullet}OH$). Finally, the superoxide ($O_2^{\bullet-}$) and hydroxyl radicals ($^{\bullet}OH$) degrade the organic molecules to simpler fragments.[105,113] This process of migration and capture of photo generated charges due to the presence of dispersed impurities improved the ($e^-/h^+$) pair separation and reduced the recombination rate, as shown in the proposed mechanism, Fig. 13.

## Conclusions

We have successfully developed a novel route to synthesize composites of graphene and $TiO_2$–$ZrO_2$ using a single-step alkaline reaction with NaOH without hazardous reducing agents. The synthesized rGO/$TiO_2$–$ZrO_2$ composites with 10–20 wt% $ZrO_2$ were successfully used for the photodegradation of MB dye under UV light. Photo-decolourization of MB solution indicated that GTZ-20 (20 wt% $ZrO_2$) had the highest activity of all the composites studied due to its superior properties/activity in the visible light range. Increasing the Zr-to-Ti/rGO ratio above 20 wt%, however, decreased the photodegradation activity of the composites. The GTZ-*X* composites possess a high photocatalytic performance toward the near UV and visible region important for efficient solar energy utilization. We believe that this work will provide a simple and efficient route to synthesize rGO/$TiO_2$–$ZrO_2$ composites with improved photocatalytic activity that have potential for treating organic pollutants in effluents.

## Conflicts of interest

There are no conflicts to declare.

## Acknowledgements

## References

1 R. Pourata, A. R. Khataee, S. Aber and N. Daneshvar, *Desalination*, 2009, **249**, 301–307.

2 B. Zielińska, J. Grzechulska and A. W. Morawski, *J. Photochem. Photobiol.*, 2003, **157**, 65–70.

3 N. Daneshvar, D. Salari and A. R. Khataee, *J. Photochem. Photobiol.*, 2003, **157**, 111–116.

4 C. Andriantsiferana, E. F. Mohamed and H. Delmas, *Environ. Technol.*, 2014, **35**, 355–363.

5 N. Daneshvar and A. R. Khataee, *J. Environ. Sci. Health A*, 2006, **41**, 315–328.

6 Y. Deng and R. Zhao, *Curr. Pollut. Rep.*, 2015, **1**, 167–176.

7 V. Etacheri, C. Di Valentin, J. Schneider, D. Bahnemann and S. C. Pillai, *J. Photochem. Photobiol., C*, 2015, **25**, 1–29.

8 D. F. Ollis, E. Pelizzetti and N. Serpone, *J. Environ. Sci. Technol.*, 1991, **25**, 1522–1529.

9 D. F. Ollis and C. Turchi, *Environ. Prog.*, 1990, **9**, 229–234.

10 R. P. S. Suri, J. Liu, D. W. Hand, J. C. Crittenden, D. L. Perram and M. E. Mullins, *Water Environ. Res.*, 1993, **65**, 665–673.

11 H.-J. Lewerenz, ed. H. O. Finklea, *Adv. Mater.*, 1989, vol. 55, pp. 96–97.

12 E. Ruiz-Hitzky, P. Aranda, M. Akkari, N. Khaorapapong and M. Ogawa, *Beilstein J. Nanotechnol.*, 2019, **10**, 1140–1156.

13 Y. Yang and C. Tian, *Res. Chem. Intermed.*, 2014, **41**, 5271–5281.

14 D. Friedmann, C. Mendive and D. Bahnemann, *Appl. Catal., B*, 2010, **99**, 398–406.

15 P. Vlazan, D. H. Ursu, C. Irina-Moisescu, I. Miron, P. Sfirloaga and E. Rusu, *Mater. Charact.*, 2015, **101**, 153–158.

16 H. Wang, L. Zhang, Z. Chen, J. Hu, S. Li, Z. Wang, J. Liu and X. Wang, *Chem. Soc. Rev.*, 2014, **43**, 5234–5244.

17 J. X. Low, J. G. Yu, M. Jaroniec, S. Wageh and A. A. Al-Ghamdi, *Adv. Mater.*, 2017, **29**, 1601694.

18 N. Setarehshenas, S. H. Hosseini and G. Ahmadi, *Arab. J. Sci. Eng.*, 2017, **43**, 5785–5797.

19 V. Vishwanathan, H. Roh, J. Kim and K. Jun, *Catal. Lett.*, 2004, **96**, 23–28.

20 K. V. R. Chary, G. V. Sagar, D. Naresh, K. K. Seela and B. Sridhar, *J. Phys. Chem. B*, 2005, **109**, 9437–9444.

21 X. Fu, L. A. Clark, Q. Yang and M. A. Anderson, *Environ. Sci. Technol.*, 1996, **30**, 647–653.

22 M. E. Manríquez, T. López, R. Gómez and J. Navarrete, *J. Mol. Catal. A: Chem.*, 2004, **220**, 229–237.

23 B. M. Reddy and A. Khan, *Catal. Rev.*, 2007, **47**, 257–296.

24 B. M. Pirzada, N. A. Mir, N. Qutub, O. Mehraj, S. Sabir and M. Muneer, *Mater. Sci. Eng., B*, 2015, **193**, 137–145.

25 J. A. Navío, M. C. Hidalgo, M. Roncel and M. A. De la Rosa, *Mater. Lett.*, 1999, **39**, 370–373.

26 J.-Y. Kim, C.-S. Kim, H.-K. Chang and T.-O. Kim, *Adv. Powder Technol.*, 2010, **21**, 141–144.

27 B. Wu, R. Yuan and X. Fu, *J. Solid State Chem.*, 2009, **182**, 560–565.

28 K. Siwinska-Ciesielczyk, A. Andrzejczak, D. Paukszta, A. Piasecki, D. Moszynski, A. Zgola-Grzeskowiak and T. Jesionowski, *Materials*, 2021, **14**, 5361.

29 M. Li, X. Li, G. Jiang and G. He, *Ceram. Int.*, 2015, **41**, 5749–5757.

30 J. Wang, Y. Yu, S. Li, L. Guo, E. Wang and Y. Cao, *J. Phys. Chem. C*, 2013, **117**, 27120–27126.

31 S. T. Pantelides, *Rev. Mod. Phys.*, 1978, **50**, 797–858.

32 Y. Qu and X. Duan, *Chem. Soc. Rev.*, 2013, **42**, 2568–2580.

33 C. N. Rao, A. K. Sood, K. S. Subrahmanyam and A. Govindaraj, *Angew. Chem.*, 2009, **48**, 7752–7777.

34 G. Lui, J.-Y. Liao, A. Duan, Z. Zhang, M. Fowler and A. Yu, *J. Mater. Chem. A*, 2013, **1**, 12255.

35  M. Huang, J. Yu, Q. Hu, W. Su, M. Fan, B. Li and L. Dong, *Appl. Surf. Sci.*, 2016, **389**, 1084–1093.

36  M. Tahir, B. Tahir, M. G. M. Nawawi, M. Hussain and A. Muhammad, *Appl. Surf. Sci.*, 2019, **485**, 450–461.

37  W. S. A. El-Yazeed and A. I. Ahmed, *Inorg. Chem. Commun.*, 2019, **105**, 102–111.

38  N. Chekir, O. Benhabiles, D. Tassalit, N. A. Laoufi and F. Bentahar, *Desalin. Water Treat.*, 2015, **57**, 6141–6147.

39  A. Yang, J. Luo and Z. Xie, *J. Mater. Res. Technol.*, 2021, **15**, 1479–1486.

40  J. Chen, H. Zheng, Y. Zhao, M. Que, W. Wang and X. Lei, *Ceram. Int.*, 2020, **46**, 20088–20096.

41  S. M. Hassan, A. I. Ahmed and M. A. Mannaa, *J. Sci.: Adv. Mater. Devices*, 2019, **4**, 400–412.

42  A. Esteves, L. C. A. Oliveira, T. C. Ramalho, M. Goncalves, A. S. Anastacio and H. W. P. Carvalho, *Catal. Commun.*, 2008, **10**, 330–332.

43  V. C. Jayawardena, D. R. Jayasundara, G. Amaratunga and V. Jayaweera, Method for the synthesis of graphene oxide, *US Pat.*, US10336619B2, 2018.

44  P. Karthik, V. Vinesh, M. Anpo and B. Neppolian, *Current Developments in Photocatalysis and Photocatalytic Materials*, Elsevier, 2020, pp. 403–416, DOI: 10.1016/b978-0-12-819000-5.00025-4.

45  L. G. Joyner, E. P. Barret and R. Skold, *J. Am. Chem. Soc.*, 1951, **1**, 373–380.

46  G. N. Shao, Y. Kim, S. M. Imran, S. J. Jeon, P. B. Sarawade, A. Hilonga, J.-K. Kim and H. T. Kim, *Microporous Mesoporous Mater.*, 2013, **179**, 111–121.

47  Y. N. Kim, G. N. Shao, S. J. Jeon, S. M. Imran, P. B. Sarawade and H. T. Kim, *Chem. Eng. J.*, 2013, **231**, 502–511.

48  A. López, D. Acosta, A. I. Martínez and J. Santiago, *Powder Technol.*, 2010, **202**, 111–117.

49  W. S. Kuo and P. H. Ho, *Chemosphere*, 2001, **41**, 77–83.

50  V. K. Gupta, R. Jain, A. Mittal, M. Mathur and S. Sikarwar, *J. Colloid Interface Sci.*, 2007, **309**, 464–469.

51  G. N. Shao, A. Hilonga, Y. N. Kim, J.-K. Kim, G. Elineema, D. V. Quang, S. J. Jeon and H. T. Kim, *Chem. Eng. J.*, 2012, **198–199**, 122–129.

52  M. H. H. Ali, A. D. Al-Afify and M. E. Goher, *Egypt. J. Aquat. Res.*, 2018, **44**, 263–270.

53  P. Srinivasu, S. P. Singh, A. Islam and L. Han, *Adv. OptoElectron.*, 2011, **2011**, 1–5.

54  H. H. Huang, K. K. H. De Silva, G. R. A. Kumara and M. Yoshimura, *Sci. Rep.*, 2018, **8**, 6849.

55  K. Mamulova Kutlakova, J. Tokarsky, P. Kovar, S. Vojteskova, A. Kovarova, B. Smetana, J. Kukutschova, P. Capkova and V. Matejka, *J. Hazard. Mater.*, 2011, **188**, 212–220.

56  A. Kambur, G. S. Pozan and I. Boz, *Appl. Catal., B*, 2012, **115–116**, 149–158.

57  X. Wang, S. O. Pehkonen, J. Rämö, M. Väänänen, J. G. Highfield and K. Laasonen, *Catal. Sci. Technol.*, 2012, **2**, 784.

58  V. Štengl, D. Popelková and P. Vláčil, *J. Phys. Chem. C*, 2011, **115**, 25209–25218.

59  L. Gu, J. Wang, H. Cheng, Y. Zhao, L. Liu and X. Han, *ACS Appl. Mater. Interfaces*, 2013, **5**, 3085–3093.

60  O. Akhavan and E. Ghaderi, *J. Phys. Chem. C*, 2009, **113**(47), 20214–20220.

61  H.-W. Tien, Y.-L. Huang, S.-Y. Yang, J.-Y. Wang and C.-C. M. Ma, *Carbon*, 2011, **49**, 1550–1560.

62  D. Yang, A. Velamakanni, G. Bozoklu, S. Park, M. Stoller, R. D. Piner, S. Stankovich, I. Jung, D. A. Field, C. A. Ventrice and R. S. Ruoff, *Carbon*, 2009, **47**, 145–152.

63  P. Xiong, S. Xu, T. Yang and K. Jing, *ACS Omega*, 2021, **6**, 28813–28827.

64  S. Gong, Z. Jiang, S. Zhu, J. Fan, Q. Xu and Y. Min, *J. Nanoparticle Res.*, 2018, **20**, 310.

65  H.-B. Kim and D.-J. Jang, *CrystEngComm*, 2015, **17**, 3325–3332.

66  K. Kim, A. Razzaq, S. Sorcar, Y. Park, C. A. Grimes and S.-I. In, *RSC Adv.*, 2016, **6**, 38964–38971.

67  Y. Xie, S. Heo, S. Yoo, G. Ali and S. Cho, *Nanoscale Res. Lett.*, 2009, **5**, 603–607.

68  M. Mikami, S. Nakamura, O. Kitao and H. Arakawa, *Phys. Rev. B: Condens. Matter Mater. Phys.*, 2002, **66**, 155213.

69  S. N. Basahel, T. T. Ali, M. Mokhtar and K. Narasimharao, *Nanoscale Res. Lett.*, 2015, **10**, 73.

70  Y. Zhao, L. Zhan, J. Tian, S. Nie and Z. Ning, *Electrochim. Acta*, 2011, **56**, 1967–1972.

71  S. Liu, L. Wang, J. Tian, Y. Luo, X. Zhang and X. Sun, *J. Colloid Interface Sci.*, 2011, **363**, 615–619.

72  J. Shen, T. Li, Y. Long, M. Shi, N. Li and M. Ye, *Carbon*, 2012, **50**, 2134–2140.

73  W.-W. L. Syafiqah, R. Binti Nazri and C.-S. Khe, *et al.*, presented in part at the 4th Electronic and Green Materials International Conference 2018 (EGM 2018), 2018.

74  D. Khalili, *New J. Chem.*, 2016, **40**, 2547–2553.

75  M. Cruz, C. Gomez, C. J. Duran-Valle, L. M. Pastrana-Martínez, J. L. Faria, A. M. T. Silva, M. Faraldos and A. Bahamonde, *Appl. Surf. Sci.*, 2017, **416**, 1013–1021.

76  L. Tan, W. J. Ong and S. P. Chai, *et al.*, *Nanoscale Res. Lett.*, 2013, **8**, 465.

77  M. Ruidíaz-Martínez, M. A. Álvarez, M. V. López-Ramón, G. Cruz-Quesada, J. Rivera-Utrilla and M. Sánchez-Polo, *Catalysts*, 2020, **10**, 520.

78  W. Li, X. Liu and H. Li, *J. Mater. Chem. A*, 2015, **3**, 15214–15224.

79  M. N. Kajama, H. Shehu, E. Okon and E. Gobina, *Energy Environ*, 2015, **5**(1), 110–120.

80  P. Makula, M. Pacia and W. Macyk, *J. Phys. Chem. Lett.*, 2018, **9**, 6814–6817.

81  R. S. Das, S. K. Warkhade, A. Kumar and A. V. Wankhade, *Res. Chem. Intermed.*, 2019, **45**, 1689–1705.

82  L. Zhang, P. Liu and Z. Su, *J. Mol. Catal. A: Chem.*, 2006, **248**, 189–197.

83  C. G. Silva and J. L. Faria, *Appl. Catal., B*, 2010, **101**, 81–89.

84  Y. Zhang, Z.-R. Tang, X. Fu and A. Y.-J. Xu, *ACS Nano*, 2010, **4**, 7303–7314.

85 K. Gurushantha, K. S. Anantharaju, L. Renuka, S. C. Sharma, H. P. Nagaswarupa, S. C. Prashantha, Y. S. Vidya and H. Nagabhushana, *RSC Adv.*, 2017, **7**, 12690–12703.

86 M. Shoeb, B. R. Singh, J. A. Khan, W. Khan, B. N. Singh, H. B. Singh and A. H. Naqvi, *Adv. Nat. Sci.: Nanosci. Nanotechnol.*, 2013, **4**, 035015.

87 J. A. Khan, M. Qasim, B. R. Singh, S. Singh, M. Shoeb, W. Khan, D. Das and A. H. Naqvi, *Spectrochim. Acta, Part A*, 2013, **109**, 313–321.

88 Z. N. Kayani, A. Kamran, Z. Saddiqe, S. Riaz and S. Naseem, *J. Photochem. Photobiol., B*, 2018, **183**, 357–366.

89 A. Juma, I. Oja Acik, A. T. Oluwabi, A. Mere, V. Mikli, M. Danilson and M. Krunks, *Appl. Surf. Sci.*, 2016, **387**, 539–545.

90 Q. Hou, C. Zhao and Z. Xu, *Chem. Phys. Lett.*, 2016, **658**, 336–342.

91 M. Acik and Y. J. Chabal, *J. Mater. Sci. Res.*, 2013, **2**, 101–112.

92 R. Molinari, C. Lavorato and P. Argurio, *Catalysts.*, 2020, **10**, 1334.

93 E. Burstein, *Phys. Rev.*, 1954, **93**, 632–633.

94 N. Sharma, S. Sharma, K. Prabakar, S. Amirthapandian, S. Ilango, S. Dash and A. K. Tyagi, *Mater. Sci., Phys.*, 2017, **2**(5), 342–346.

95 A. J. Antony, S. M. Jelastin Kala, C. Joel, R. B. Bennie and S. Praveendaniel, *J. Phys. Chem. Solids*, 2021, **157**, 110169.

96 J. B. Coulter and D. P. Birnie, *Phys. Status Ssolidi B*, 2018, **255**, 1700393.

97 A. Dhanaraj, K. Das and J. M. Keller, *AIP Conf.: Proce.*, 2020, **2270**, 110040.

98 A. S. Hassanien and A. A. Akl, *J. Alloys Compd.*, 2015, **648**, 280–290.

99 B. Choudhury and A. Choudhury, *Phys. E*, 2014, **56**, 364–371.

100 S. D. Perera, R. G. Mariano, K. Vu, N. Nour, O. Seitz, Y. Chabal and K. J. Balkus, *ACS Catal.*, 2012, **2**, 949–956.

101 Y. Zhang and C. Pan, *J. Mater. Sci. Res*, 2010, **46**, 2622–2626.

102 Y. Yang, L. Xu, H. Wang, W. Wang and L. Zhang, *Mater. Des.*, 2016, **108**, 632–639.

103 Y. Xua and C. H. Langford, *J. Photochem. Photobiol., A*, 2000, **133**, 67–71.

104 A. Mills and S. L. Hunte, *J. Photochem. Photobiol., A*, 1997, **108**, 1–35.

105 T. V. L. Thejaswini, D. Prabhakaran and M. A. Maheswari, *J. Photochem. Photobiol., A*, 2017, **344**, 212–222.

106 H. Lv, X. Wu, Y. Liu, Y. Cao and H. Ren, *Mater. Lett.*, 2019, **236**, 690–693.

107 J. Li, F. Wei, C. Dong, W. D. Mu and X. Han, *J. Mater. Chem. A*, 2020, **8**, 6524–6531.

108 N. Shehzad, M. Tahir, K. Johari, T. Murugesan and M. Hussain, *Appl. Surf. Sci.*, 2019, **463**, 445–455.

109 R. R. Ikreedeegh and M. Tahir, *Fuel*, 2021, **305**, 121558.

110 J. Liu, X. Meng, Y. Hu, D. Geng, M. N. Banis, M. Cai, R. Li and X. Sun, *Carbon*, 2013, **52**, 74–82.

111 A. Ajmal, I. Majeed, R. N. Malik, H. Idriss and M. A. Nadeem, *RSC Adv.*, 2014, **4**, 37003–37026.

112 A. S. Kshirsagar and P. K. Khanna, *Inorg. Chem. Front.*, 2018, **5**, 2242–2256.

113 S. Liu, G. Ren, X. Gao, Z. Li, L. Wang and X. Meng, *Chem. Commun.*, 2022, **58**, 8198–8201.